

Modeling Investigation of the Stability and Irradiation-Induced Evolution of Nanoscale Precipitates in Advanced Structural Materials

**Fuel Cycle/Reactor Concepts
Mission Relevant Investigator Initiated Research**

Dr. Brian Wirth
University of Tennessee Knoxville

Sue Lesica, Federal POC
Jeremy Busby, Technical POC

**FINAL REPORT FOR
U.S. DEPARTMENT OF ENERGY NUCLEAR ENERGY UNIVERSITY PROGRAMS
Project 10-906**

Project Title: Modeling investigation of the stability and irradiation-induced evolution of nanoscale precipitates in advanced structural materials

Technical Work Scope: MR-IIR

Papers and Publications:

A. Certain, H.-J. Lee Voigt, T.R. Allen, and B.D. Wirth, “Investigation of cascade-induced resolution from nanometer sized coherent precipitates in dilute Fe-Cu alloys”, *Journal of Nuclear Materials* **432** (2013) 281-286.

T.L. Hoang, A. Arsenlis, H.J. Lee-Voigt, D.C. Chrzan, and B.D. Wirth, “Atomistic Study of Eshelby’s inclusion and inhomogeneity problems in a model bcc crystal”, *Modeling and Simulation in Materials Science and Engineering* **19** (2011) 085001.

Invited & Contributed Oral Presentations:

B.D. Wirth, A. Certain and D. Xu, “Multiscale Modeling of Precipitate Stability in Irradiated Structural Materials, ”, TMS 2014 annual meeting Symposium on Computational Thermodynamics and Kinetics, San Diego, CA, 20 February 2014, **(invited)**.

B.D. Wirth, A.G. Certain, and D. Xu, “Multiscale Modeling of Nanoscale Precipitate Stability in Irradiated Structural Materials”, TMS 2013 Symposium on Computational Thermodynamics and Kinetics, San Antonio, TX, 5 March 2013, **(invited)**.

B.D. Wirth, K. Hammond, N. Camilli, L. Marus, N. Juslin, H.-J.L. Voigt, and A. Certain, “Character & Composition of Nanoscale Y-Ti-O Precipitates in Advanced Oxide Dispersion Strengthened Steels”, Oxford University Workshop on Oxide Dispersion Strengthened Steels, 25 September 2012.

B.D. Wirth, K. Hammond, N. Juslin, L. Marus, H.-J. L. Voigt, and A. Certain, “Atomic Scale Investigation of Y-Ti-O Nanoclusters in Nanostructured Ferritic Alloys”, 2011 TMS Annual Meeting, Symposium on Approaches for Investigating Phase Transformations at the Atomic Scale, San Diego, CA, 1 March 2011.

Motivation and Objectives

Materials used in extremely hostile environment such as nuclear reactors are subject to a high flux of neutron irradiation, and thus vast concentrations of vacancy and interstitial point defects are produced because of collisions of energetic neutrons with host lattice atoms. The fate of these defects depends on various reaction mechanisms which occur immediately following the displacement cascade evolution and during the longer-time kinetically dominated evolution such as annihilation, recombination, clustering or trapping at sinks of vacancies, interstitials and their clusters. The long-range diffusional transport and evolution of point defects and self-defect clusters drive a microstructural and microchemical evolution that are known to produce degradation of mechanical properties including the creep rate, yield strength, ductility, or fracture toughness, and correspondingly affect material serviceability and lifetimes in nuclear applications. Therefore, a detailed understanding of microstructural evolution in materials at different time and length scales is of significant importance. The primary objective of this work is to utilize a hierarchical computational modeling approach i) to evaluate the potential for nanoscale precipitates to enhance point defect recombination rates and thereby the self-healing ability of advanced structural materials, and ii) to evaluate the stability and irradiation-induced evolution of such nanoscale precipitates resulting from enhanced point defect transport to and annihilation at precipitate interfaces.

This project will utilize, and as necessary develop, computational materials modeling techniques within a hierarchical computational modeling approach, principally including molecular dynamics, kinetic Monte Carlo and spatially-dependent cluster dynamics modeling, to identify and understand the most important physical processes relevant to promoting the “self-healing”, or radiation resistance in advanced materials containing nanoscale precipitates. In

particular, the interfacial structure of embedded nanoscale precipitates will be evaluated by electronic- and atomic-scale modeling methods, and the efficiency of the validated interfaces for trapping point defects will next be evaluated by atomic-scale modeling (e.g., determining the sink strength of the precipitates), addressing key questions related to the optimal interface characteristics to attract point defects and enhance their recombination. Kinetic models will also be developed to simulate microstructural evolution of the nanoscale features and irradiation produced defect clusters, and compared with observed microstructural changes.

Project Results:

Precipitation often occurs in materials that contain one or more solute elements, and is of particular significance in the field of nuclear structural materials. Due to the creation and accumulation of defects (e.g., vacancies, interstitials and their clusters) under irradiation, structural materials in nuclear reactors are subject to a host of irradiation effects, such as irradiation hardening, irradiation embrittlement and irradiation creep, which can severely deteriorate the designed properties of these materials [1-4]. One strategy developed in the past decades to mitigate the detrimental irradiation effects is to introduce a high number density of fine nanoscale particles through thermal precipitation prior to the deployment of the materials in nuclear reactors [5]. Such precipitates enhance recombination of vacancies and interstitials during irradiation, reduce the net accumulation of irradiation defects, and therefore, alleviate irradiation damage to the microstructure and properties of the matrix material. In addition, these precipitates also provide better design properties (e.g., higher strength, higher creep resistance) to the matrix material.

On the other hand, undesirable precipitation can take place in nuclear structural materials during the course of irradiation. Copper rich precipitates and nickel-manganese rich precipitates

("late blooming phase") have been found to form in reactor pressure vessel (RPV) steels during service and been considered leading factors in the observed embrittlement of the materials [6-8]. Precipitation of carbides, phosphides, silicides etc. has been observed in fast reactor irradiated stainless steels and correlated to measured property degradation [9,10]. Some of the precipitate phases observed after irradiation are favored by equilibrium thermodynamics, while others are not. The formation of the former is possible under pure thermal conditions but is accelerated under irradiation, while the latter can only be formed under non-equilibrium conditions such as irradiation.

Since precipitates have a large impact on materials properties, whether in a favored or undesired direction, it is important to develop computational models that can reliably predict the quantitative characteristics of precipitates, mean size and number density, for instance. These quantities depend on processing/application conditions (temperature, irradiation dose rate and dose etc.) and duration. For example, irradiation may not only introduce new precipitates, but may also modify pre-existing precipitates, causing them either to shrink or coarsen in size.

The basic atomistic mechanisms underlying the precipitation phenomenon are the diffusion and interactions of solute atoms. When a monomer solute atom encounters another along its diffusion path, the two monomers combine to form a dimer, and when a dimer is approached by a diffusing monomer they combine to form a trimer, and so on. This clustering process leads to a continuous growth in size space and to the formation of precipitates that are big enough to be detected by various characterization techniques. In the inverse direction, a dimer, a trimer or a bigger precipitate can emit monomers as a result of thermal activation or ballistic collisions. This emission process leads to a reduction in cluster sizes and re-dissolution of solute atoms from precipitates into the matrix.

The basic atomistic mechanisms underlying the precipitation phenomenon are the diffusion and interactions of solute atoms. When a monomer solute atom encounters another along its diffusion path, the two monomers combine to form a dimer, and when a dimer is approached by a diffusing monomer they combine to form a trimer, and so on. This clustering process leads to a continuous growth in size space and to the formation of precipitates that are big enough to be detected by various characterization techniques. In the inverse direction, a dimer, a trimer or a bigger precipitate can emit monomers as a result of thermal activation or ballistic collisions. This emission process leads to a reduction in cluster sizes and re-dissolution of solute atoms from precipitates into the matrix.

In a recent study, Certain et al. performed molecular dynamics (MD) simulations of cascade induced re-dissolution of copper precipitates in an iron matrix and developed through statistical analysis of the MD results a cascade re-dissolution parameter defined as the number of re-dissolved Cu atoms per cluster (precipitate) atom per collision event [11]. The cascade re-dissolution parameter provides a new opportunity to fully quantitatively assess the ballistic effect on the precipitation/re-dissolution kinetics under irradiation.

In this report, we present an experimentally validated computational investigation on the Cu precipitation/re-dissolution kinetics in a Fe-0.78at%Cu model alloy under thermal and/or irradiation conditions, which represent the outcome of NEUP project 10-906. The subject alloy and the Cu precipitation are relevant to the important issue of RPV steel embrittlement. The experimental part of this work involves thermal anneal, ion irradiation and precipitate characterization by atom probe tomography (APT), while the computational part concerns developing, calibrating and validating through comparison with the APT experiments a set of diffusion-reaction rate theory based cluster dynamics models for the Cu precipitation/re-

dissolution under thermal and/or irradiation conditions, as well as using the models to gain mechanistic insights into the complex phenomena. The aforementioned cascade re-dissolution parameter, as well as irradiation enhanced diffusivity of copper monomers, is incorporated in the irradiation model.

Experiments for model validation:

Four specimens of Fe-0.78at%Cu were pre-annealed at 450°C under vacuum for 24 hours to thermally grow Cu precipitates. Three of the pre-annealed specimens were then exposed to a 5 MeV Ni ion beam with an ion flux of $9.8 \times 10^{12} \text{ cm}^{-2} \text{ s}^{-1}$ for 7 hours at the Environmental Molecular Sciences Laboratory (EMSL) of the Pacific Northwest National Laboratory. Three different temperatures, -20, 300, and 600 °C, were used for the irradiation specimens, respectively. During the irradiation of each specimen, half of the specimen surface was shielded from irradiation, providing an unirradiated control subjected to the same secondary thermal anneal at each temperature. For clarity purpose, we define three sets of specimens: Set I, the solely pre-annealed specimen; Set II, the unirradiated parts of the irradiation specimens which experienced both the pre-anneal and the secondary anneal but not the irradiation; Set III, the irradiated parts of the irradiation specimens which experienced the pre-anneal, the secondary anneal, and the ion irradiation.

Atom probe tomography (APT) was performed on all the three sets of specimens to detect and measure the average radius and the number density of possible copper precipitates resulting from each different processing condition/history. In particular, for the Set III specimens, small samples for APT were extracted from a depth of 0.5 μm below the irradiated surface, using the focused ion beam (FIB) technique. Calculation with SRIM 2008 [12] in the

quick Kinchin-Pease mode suggests a nominal dose rate of 3.48×10^{-3} dpa s⁻¹ at this depth, and a nominal dose of ~88 dpa at the end of the 7 hr irradiation. These nominal values of dose rate and dose only serve as a quick reference in future comparison with other experiments, and are not used in the detailed modeling part of this study. A more careful account of defect production combining SRIM primary knock-on atom (PKA) energy distribution and molecular dynamics (MD) cascade simulation results will be used in the modeling instead.

Experimental results

The APT measured average radius and number density of Cu precipitates in the different specimens and the qualitative (re-dissolved or coarsened) changes with respect to the Set I specimen are presented in Table 1. The solely pre-annealed specimen (Set I) exhibited a number density of Cu precipitates of 5.1×10^{-4} nm⁻³, with an average radius of 1.3 nm. Small angle neutron scattering (SANS) had been previously performed on a specimen with the same composition and processing history, yielding a number density of Cu precipitates of 9×10^{-4} nm⁻³, and an average radius of 0.9 nm, as included in the square brackets in Table 1. Comparison of the two sets of data for the same specimen/history gives a hint of the level of uncertainty associated with the APT measurements.

The Set II specimens that were subjected to secondary anneals at -20 and 300 °C did not show noticeable changes in either the average radius or the number density of Cu precipitates with respect to the Set I specimen, suggesting the 7 hr secondary anneals at these two temperatures had no effect on the precipitates that formed during the 24 hr pre-anneal at 450 °C.

The Set II specimen subjected to a secondary anneal at 600 °C showed no precipitates as detected by APT. This could be interpreted in two different ways. One possibility is that the pre-

anneal formed precipitates were fully re-dissolved into the matrix, or to a lesser degree of re-dissolution, the sizes of the precipitates were all reduced to below the size-detection limit (~ 0.5 nm radius) of the atom probe used. The other possibility is that the pre-anneal formed precipitates underwent severe coarsening which significantly cut down the number density of precipitates at the same time of increasing the precipitate size. Due to the small volume (a few 10^5 nm³) of material an atom probe handles, precipitates at a very low density (10^{-6} - 10^{-5} nm⁻³) may simply not be represented in an APT sample.

The Set III specimen irradiated at -20 °C for 7 hr showed a number density of precipitates of 3.8×10^{-4} nm⁻³ and an average radius of 0.6 nm, both lower than those exhibited by the Set I specimen. This clearly suggests that the irradiation at this low temperature led to a net, although not complete, re-dissolution of Cu atoms from the pre-anneal formed precipitates back into the matrix.

The Set III specimen irradiated at 300 °C for 7 hr showed a number density of precipitates about one order of magnitude lower than the Set I specimen, and an average precipitate size about double that exhibited by the Set I specimen. This indicates that the irradiation at 300 °C resulted in coarsening of the pre-anneal formed precipitates.

Same as the Set II specimen subjected to a secondary anneal at 600 °C for 7 hours (without irradiation), the Set III specimen irradiated at 600 °C for 7 hours exhibited no Cu precipitates as detected by APT. As discussed earlier, this could be interpreted as resulting from either significant re-dissolution or severe coarsening of the pre-anneal formed precipitates. In view of the apparent coarsening of the precipitates in the Set III specimen irradiated at 300 °C, however, it is more tempting here to speculate that coarsening also occurred in this specimen irradiated at 600 °C.

Basic model construct

As illustrated in Fig. 1, the precipitation/re-dissolution behavior is governed by the competition between two basic kinetic processes: capturing (or, clustering) that leads to the increment of the Cu precipitate size as indicated by the right-pointing arrows, and emission that decreases the precipitate size as indicated by the left-pointing arrows.

Capturing occurs when a precipitate (Cu cluster, immobile) is approached by a migrating monomer Cu atom (substitutional solute, migrating through a vacancy mechanism), or two migrating monomers encounter each other. Emission occurs when a monomer Cu atom is released from a precipitate/cluster due to thermal activation or through a ballistic collision event.

In the field of nuclear materials, a classical rate theory framework has been established to treat similar capturing and emission processes occurring among irradiation defects, such as vacancies, interstitials and their various forms of clusters [1-2,13-15]. In the framework, a capturing process is treated as a second order chemical reaction, whose rate is proportional to the product of the number densities (concentrations) of the two reacting species, and an emission process is treated as a first order chemical reaction, with a rate proportional to the number density of the parent species. Here we borrow this framework and use it for the Cu precipitation and re-dissolution kinetics.

The equation that describes the changing rate of the number density (C_n) of the precipitates/clusters made up of n -Cu ($n>1$) atoms is written as

$$\left\{ \frac{\partial C_n}{\partial t} = k_{n-1}^+ C_1 C_{n-1} + k_{n+1}^- C_{n+1} - k_n^+ C_1 C_n - k_n^- C_n \right\} \quad (1),$$

where k_n^+ and k_n^- are the rate constants for the n -Cu clusters capturing and emitting Cu monomers, respectively. The braces in Eq. (1) are used to imply that there is one such equation

for each cluster size (n , greater than 1) and that the equations for different cluster sizes are coupled and they all belong to a system of equations.

The equation for the Cu monomers ($n=1$) differs from Eq. (1) and is written as

$$\frac{\partial C_1}{\partial t} = 2 \times k_2^- C_2 + \sum_{n>2} k_n^- C_n - 2 \times k_1^+ C_1^2 - \sum_{n>1} k_n^+ C_1 C_n \quad (2).$$

Monomers can be emitted by all different sized clusters ($n>1$) and can be captured by all clusters as well as monomers. The factor of 2 in Eq. (2) is needed due to the fact that two monomers are involved in one event of $Cu + Cu \rightleftharpoons Cu_2$ proceeding in either direction. It is worth noting that

Eqs. (1-2) strictly satisfy the conservation of Cu monomers, i.e., $\sum_{m=1}^{\infty} m \times \frac{\partial C_m}{\partial t} = 0$, which can be easily proved.

After the establishment of Eqs. (1-2), three other constituents are needed in order to form a complete model for a specific problem. These are: 1). expression of the capturing rate constant k_n^+ , 2). expression of the emission rate constant k_n^- , and 3). initial conditions (i.e., initial number densities of all different sized Cu-species including monomers and clusters).

As will be seen later, k_n^- expression and initial conditions may be case (pre-anneal, secondary anneal and/or irradiation) specific, and hence will be discussed in respective sections. However, a common expression,

$$k_n^+ = 4\pi(r_1 + r_n)(D_1 + D_n) \quad (3),$$

of the capturing rate constant, where r is the radius, and D is the diffusivity, can be used for all the cases in this study. This expression was derived for diffusion driven reactions in the classical rate theory [1-2]. Since only Cu monomers are considered mobile ($D_{n>1} = 0$), this expression can

be further written as: $k_1^+ = 16\pi r_1 D_1$ for monomer-monomer capturing interaction, and $k_{n>1}^+ = 4\pi(r_1 + r_n)D_1$ for monomer-cluster ($n>1$) capturing interaction.

The capturing rate constant k_n^+ requires r_n (including $n=1$) and D_1 as input parameters. The radius of a Cu-cluster r_n can be easily related to the number of monomers contained in the cluster, i.e., the n number, by treating a cluster as a sphere. This is irrespective of processing conditions. The diffusivity of Cu monomers, D_1 , however, needs to be treated differently for thermal and irradiation conditions, as to be discussed in the next sections.

Model for the Set I specimen (pre-anneal only)

In the pre-anneal case, the emission of monomers from a cluster ($n>1$) is solely driven by thermal activation. Based on the concept of detailed balance, the classical rate theory expresses the thermal emission rate constant as $k_n^- = k_{n-1}^+ C_0 \exp\left(-\frac{E_n^B}{k_B T}\right)$ (defined for $n>1$ only; no emission is from monomers), where C_0 is the atomic number density of the matrix, and E_n^B is the binding energy of a Cu monomer to an n -Cu ($n>1$) cluster. Substituting Eq. (3) here for k_{n-1}^+ , this becomes

$$k_n^- = 4\pi(r_1 + r_{n-1})(D_1 + D_{n-1})C_0 \exp\left(-\frac{E_n^B}{k_B T}\right) \quad (4).$$

The initial condition for the pre-anneal case is

$$\begin{cases} C_1(0) = 0.0078C_0 \\ C_{n>1}(0) = 0 \end{cases} \quad (5),$$

where C_0 is the same as defined above.

Eqs. (1-5) constitute a complete model for the pre-anneal case. The input parameters required by this model include monomer diffusivity D_1 and monomer-cluster binding energy E_n^B ($n>1$). In a pure thermal case, $D_1 = D_{thermal} = D_0 \exp\left(-\frac{E_m}{k_B T}\right)$, where D_0 is a pre-factor and E_m is the migration energy. Previous studies reported values of 0.4-0.6 $\text{cm}^2 \text{s}^{-1}$ for D_0 and 2.3-2.5 eV for E_m (e.g. [16,17]). In this study we fix D_0 to be 0.5 $\text{cm}^2 \text{s}^{-1}$, and adjust/calibrate E_m near the 2.3-2.5 eV range using the APT data for the Set I specimen. The monomer-cluster binding energy E_n^B is defined as the formation energy difference before and after the emission of a monomer from the cluster, i.e., $E_n^B = E_{n-1}^F + E_1^F - E_n^F$, and, according to the classical rate theory, can be approximated by the capillary law, i.e., $E_n^B = E_1^F + (E_2^B - E_1^F) \left[n^{2/3} - (n-1)^{2/3} \right] / (2^{2/3} - 1)$, which requires only two input parameters, Cu-monomer formation energy E_1^F in the iron matrix, and the monomer-dimer binding energy E_2^B . Values of ~ 0.5 eV and ~ 0.15 eV were previously reported (e.g. [17]) for E_1^F and E_2^B , respectively. Here we also treat E_1^F and E_2^B as calibration parameters which are adjusted around the literature values.

To compare model predictions with experimental measurements, it is important to screen the model results with a suitable size-resolution limit, and only count those clusters above the limit in the calculation of model predicted average radius and number density (posterior to the full resolution modeling), since in experiments only those precipitates big enough can be resolved. The size-resolution limit in this study is determined to be about 0.5 nm in radius, based on the raw APT data.

A calibrated set of parameters, namely, $E_m = 2.32$ eV, $E_1^F = 0.435$ eV and $E_2^B = 0.18$ eV, are obtained after many iterations of model calculation, comparison with the APT data under the

same pre-anneal condition (450 °C, 24 hrs), and manually adjusting the three parameters. The average radius and the number density of precipitates predicted by the model with the calibrated parameters are 1.2 nm and $6 \times 10^{-4} \text{ nm}^{-3}$, respectively, very close to the APT measured 1.3 nm and $5.1 \times 10^{-4} \text{ nm}^{-3}$. It is interesting to note that, despite that only two measured data points (one for average radius, the other number density) are used to calibrate three parameters, the model-experiment comparison is fairly sensitive to all the three parameters. The calibrated parameter values, however, are not guaranteed to be the most accurate. They will be tested against the Set II specimens, as detailed in the next section.

Model for the Set II specimens (pre-anneal + secondary anneal)

The Set II specimens were subjected to a 7 hr secondary anneal, at -20, 300, 600 °C, respectively, after the pre-anneal at 450 °C for 24 hrs. The precipitation/re-dissolution kinetics in these specimens is purely driven by thermal activation, same as in the Set I specimen. Hence the model for these specimens shares with the model for the Set I specimen the same rate equations (Eqs. 1-2), and expressions of monomer capturing (Eq. 3) and monomer emitting (Eq. 4) rate constants. However, instead of that described by Eq. (5), the initial condition for the Set II specimens is the state (i.e., number densities of all different sized clusters and monomers) reached at the end of the 24 hr pre-anneal at 450 °C, which is represented by the thicker solid line (in blue) in Fig. 2.

Figure 2 also presents the number density of different sized precipitates at the end of the three secondary anneals obtained from the model for the Set II specimens. The curves (dashed in Fig. 2) for the two specimens with a secondary anneal temperature of -20 and 300 °C completely overlap the curve for the ending state of the pre-anneal which is also the starting state of the

secondary anneals. This clearly shows that the secondary anneals at these two lower temperatures have no impact on the pre-anneal formed precipitates, consistent with the APT experiments. This is further confirmed by the invariant average radius and number density extracted from the model results for these two Set II specimens, as listed in Table 2.

The thin solid line (red) in Fig. 2 shows that the Set II specimen with a secondary anneal temperature of 600 °C experiences Ostward ripening (coarsening), displaying a low lying and much broader density vs. radius profile. As listed in Table 2, the model predicted average precipitate radius for this specimen is 3.7 nm, considerably larger than the 1.2 nm (model predicted) at the start of the secondary anneal. The number density the model predicted for this specimen is $1.6 \times 10^{-5} \text{ nm}^{-3}$, more than one order of magnitude lower than the starting $6 \times 10^{-4} \text{ nm}^{-3}$. Since APT handles very small material volume on the order of a few 10^5 nm^3 or less, it is possible that the precipitates at this low number density are not represented in the small APT sample. This appears to be consistent with the fact that no precipitates were detected by APT in this specimen.

Model for the Set III specimens (pre-anneal + secondary anneal + irradiation)

The Set III specimens were subjected to the pre-anneal, the secondary anneal and the ion irradiation. Irradiation has two major effects on the precipitation kinetics, namely, cascade re-dissolution of precipitates and irradiation enhanced diffusivity of Cu monomers.

Based on MD simulations of PKA and precipitate interactions, Certain et al. developed a re-dissolution parameter defined as the number of re-dissolved Cu atoms per cluster (precipitate) atom per collision event [11] which they plotted as a function of initial PKA energy for 1, 3 and 5 nm diameter precipitates in the Fig. 7 therein. Ignoring the weak dependence of this parameter

on the initial PKA energy, and multiplying this parameter with the number of Cu-monomers in the 1, 3, and 5 nm diameter precipitates, we find that for all the studied precipitate sizes, approximately one Cu monomer is re-dissolved from a precipitate per PKA (collision event). Using this size-independent approximation of *one re-dissolution per PKA* (called *SIAD* hereafter), the rate, in the unit of one per second, of monomers being re-dissolved by cascades from a precipitate, which adds to the thermal emission rate of the precipitate, has a numerical value equal to the rate of creation of qualified PKAs around the vicinity of the precipitate. According to the Ref. [11], only those PKAs with an energy no less than 1 keV and located inside the precipitate or within a distance of one lattice parameter outside the precipitate contribute to the cascade re-dissolution mechanism. Considering these details and combining thermal and cascade effects, the net monomer-emission rate constant for the Set III specimens is written as

$$k_n^- = 4\pi(r_1 + r_{n-1})(D_1 + D_{n-1})C_0 \exp\left(-\frac{E_n^B}{k_B T}\right) + SIAD \times \frac{4\pi}{3}(r_n + a_0)^3 \times \phi \times \frac{\partial^2 N_{PKA \geq 1keV}}{\partial l \partial N_{ion}} \quad (6),$$

where a_0 is the lattice constant of the iron matrix, ϕ is the ion flux (9.8×10^{-2} ion nm⁻² s⁻¹), and

$\frac{\partial^2 N_{PKA \geq 1keV}}{\partial l \partial N_{ion}}$ is the number of PKAs (≥ 1 keV) created per ion per unit depth around the APT

examined depth (0.5 μ m) which can be obtained by running SRIM [12] in the full cascade mode for 5 MeV Ni ion implantation into iron (displacement energy 40 eV), and performing statistical

analysis of the SRIM output file “COLLISON.txt”. Here we find $\frac{\partial^2 N_{PKA \geq 1keV}}{\partial l \partial N_{ion}} \approx 0.032$ PKA per

nanometer per ion. Note that SRIM has been known to have the problem of reporting incorrect number of displacements [18] when running in a full cascade mode, but here we are using the SRIM PKA data instead of the SRIM reported displacements. Also note that we are neglecting

the influence of the precipitates on the generation of PKAs, which is a reasonable approximation considering the low total concentration (0.78 at.%) of Cu atoms.

Irradiation enhanced diffusivity of Cu monomers can be treated as

$$D_1^{irr} = D_{thermal} \frac{C_v}{C_v^{eq}} \quad (7),$$

where $D_{thermal}$ is the thermal diffusivity of Cu monomers as used for the Set I and Set II specimens, and C_v and C_v^{eq} are the vacancy concentration under irradiation and thermal equilibrium, respectively. The equilibrium vacancy concentration is determined by the vacancy formation energy E_v^F as $C_v^{eq} = C_0 \exp\left(-\frac{E_v^F}{k_B T}\right)$. A range of E_v^F values, ~ 1.6 - 2.2 eV, can be found in the literature, obtained from experiments, ab initio, or MD studies (e.g. [19-21]), and here we choose to use 1.7 eV. To calculate the vacancy concentration (averaged over the 7 hr irradiation period) under irradiation, separate defect (vacancy, interstitial, and their respective clusters) cluster dynamics modeling is carried out that takes into account intra-cascade defect-cluster production and cluster mobility, in a similar way to that described in [13]. The differences between here and Ref. [13] include: 1. material and material/irradiation related quantities (listed in Table 3), 2. negligence of the spatial dependence (weak around the depth of $0.5 \mu\text{m}$) of defect evolution in this study (bulk ion irradiation), and 3. negligence of mobility of interstitial clusters bigger than I_{20} for simplicity. Note that the production rates (listed in Table 3) of small defects/defect-clusters are obtained by combining SRIM PKA (around the $0.5 \mu\text{m}$ depth) energy data with PKA energy-dependent intra-cascade production probabilities from previous MD studies, as detailed in [13].

The average vacancy concentration obtained this way is 10 , 10^{-5} , 10^{-6} nm^{-3} , for the specimens irradiated at -20 , 300 and $600 \text{ }^\circ\text{C}$, respectively. Apparently the 10 nm^{-3} for the $-20 \text{ }^\circ\text{C}$

is too large to be physical, considering the iron atomic number density of 84.6 nm^{-3} . Before reaching this large concentration, spatial correlation among vacancies and interstitials/interstitial-clusters should have already intervened, but this cannot be treated by cluster dynamics models which are based on random mean field theory. Hence, we estimate the vacancy concentration for the $-20 \text{ }^{\circ}\text{C}$ irradiation by extrapolating the concentrations for 300 and $600 \text{ }^{\circ}\text{C}$ according to an Arrhenius relationship, and we find 0.0346 nm^{-3} .

Eqs. (1-3,6,7) plus the same initial condition as for the Set II specimens (i.e., the state reached at the end of the 24 hr pre-anneal at $450 \text{ }^{\circ}\text{C}$) constitute a complete model for the Set III specimens. The evolution of precipitate number density vs. radius predicted by this model is presented in Fig. 3 and 4, for the specimens irradiated at -20 and $300 \text{ }^{\circ}\text{C}$, respectively. The evolution for the specimen irradiated at $600 \text{ }^{\circ}\text{C}$ is qualitatively similar to that shown in Fig. 4 and hence not plotted.

As shown in Fig. 3, the irradiation at $-20 \text{ }^{\circ}\text{C}$ significantly reduces the number density of the bigger precipitates, which is because of the cascade re-dissolution mechanism. It is interesting to note that Fig. 3 also shows a decrease in the Cu monomer number density. This is because the remaining monomers in the matrix at the end of the pre-anneal acquire an enhanced diffusivity under irradiation and hence are captured by small to intermediate sized precipitates. This loss of monomers from the matrix cannot be compensated by the cascade re-dissolved monomers from the bigger precipitates which are also subject to capturing by small to intermediate sized precipitates. It is important to note that Eq. (6) shows that the cascade re-dissolution rate has a pronounced dependence ($\sim r^3$) on the size of a precipitate, which implies that, for this specimen irradiated at $-20 \text{ }^{\circ}\text{C}$ where thermal effects are weak, growth due to irradiation enhanced monomer diffusion dominates the fate of small precipitates, although

shrinkage due to cascade re-dissolution dominates the fate of the bigger precipitates. It can be expected that as irradiation continues indefinitely (beyond the 7 hour), a static profile of PPT number density vs. radius will be established due to the balance of these two factors. Compared with the initial condition at the start of irradiation, the model predicts an overall re-dissolution behavior of the pre-anneal formed precipitates in this specimen. As listed in Table 4, the model predicts an average PPT radius of 0.7 nm and a PPT number density of $5.6 \times 10^{-4} \text{ nm}^{-3}$ at the end of the 7 hr irradiation, compared to the 1.2 nm and $6 \times 10^{-4} \text{ nm}^{-3}$ (model predicted) at the start of the irradiation. The APT measured average PPT radius and PPT number density for this irradiated specimen are 0.6 nm and $3.8 \times 10^{-4} \text{ nm}^{-3}$, respectively, as shown in Table 1, which are fairly close to the model predictions, considering the level of uncertainty associated with the APT data.

The behavior of the specimen irradiated at 300 °C, shown in Fig. 4, appears quite different. Both the monomer and the small to intermediate-sized pre-existing precipitates experience a significant decrease in the number density within the 7 hr irradiation. The profile of the number density vs. radius is shifted to the lower right as new bigger precipitates are formed, at the cost of the smaller precipitates. This is a typical characteristic of Ostwald ripening. According to the Set II specimen subjected to the secondary anneal at the same temperature for the same 7 hours but without irradiation, thermal effects alone are not able to modify the profile of the pre-existing precipitates at 300 °C. On the other hand, the Set III specimen subjected to the same level of irradiation but at -20 °C shows a distinct re-dissolution behavior. These imply that in this specimen irradiated at the 300 °C, thermal effects, namely, thermal diffusion and thermal emission, are operating together with the irradiation effects, producing a net result of an enlarged (size) range of dominance of growth with respect to shrinkage as shown in Fig. 4. However, due

to the rapid increase of the cascade re-dissolution rate constant with precipitate size as depicted by Eq. (6), it can still be expected that the evolution of the profile of number density vs. radius will come to a stop after a sufficiently long time of irradiation. The average PPT radius and number density predicted by the model for this specimen at the end of the 7 hr irradiation are, respectively, 3.2 nm and $4.9 \times 10^{-5} \text{ nm}^{-3}$, as listed in Table 4, fairly close to the experimentally measured 2.5 nm and $3.5 \times 10^{-5} \text{ nm}^{-3}$.

The specimen irradiated at 600 °C behaves similar to the one irradiated at 300 °C, both experiencing obvious coarsening. Mechanistically, this specimen is also controlled by both the thermal and the irradiation effects, although the contribution from the former increases due to the higher temperature. The model predicts a fairly large average PPT radius of 13.6 nm and a very low number density of $3.6 \times 10^{-7} \text{ nm}^{-3}$. Such a low number density makes it nearly impossible to capture/include a single PPT in a small APT sample. This is consistent with the fact that no PPTs were found by APT in this specimen.

Conclusions

We have performed thermal anneal, ion irradiation and atom probe tomography (APT) experiments and cluster dynamics modeling to study the Cu precipitation/re-dissolution kinetics in irradiated and un-irradiated Fe-0.78at.%Cu. Three sets of specimens with distinct processing history were examined: Set I only subjected to a pre-anneal at 450 °C for 24 hr; Set II subjected to the pre-anneal plus a secondary anneal at -20, 300 or 600 °C; Set III subjected to the pre-anneal, the secondary anneal, and a 5 MeV Ni ion irradiation at -20, 300 or 600 °C. The APT data for the Set I specimen were used to calibrate three key parameters for the thermally activated atomistic processes (diffusion and thermal emission), yielding a Cu monomer thermal

migration energy of 2.32 eV, a Cu monomer formation energy of 0.435 eV, and a Cu monomer-to-dimer binding energy of 0.18 eV. The secondary anneal precipitation model and the irradiation precipitation model using the calibrated parameters produced good agreement with the APT experiments on the final precipitate size and number density, as well as the re-dissolution or coarsening behavior of the pre-anneal formed precipitates, in the Set II and Set III specimens. Irradiation enhanced Cu-monomer diffusion and cascade re-dissolution were both explicitly included in the irradiation precipitation model, which provided mechanistic insights into the complex interplay between the thermal and the irradiation effects on the Cu precipitation/re-dissolution kinetics.

References

1. Olander DR. Fundamental Aspects of Nuclear Reactor Fuel Elements. ERDA; 1976.
2. Was GS. Fundamentals of Radiation Materials Science: Metals and Alloys. New York: Springer; 2007.
3. Zinkle SJ, Busby JT. Mater Today 2009;12:12.
4. Allen TR, Busby JT. JOM 2009;61:29.
5. Odette GR, Alinger MJ, Wirth BD. Annu Rev Mater Res 2008;38:471.
6. Odette GR. Scripta Metall 1983;17:1183.
7. Nagai Y, Tang Z, Hasegawa M, Kanai T, Saneyasu M. Phys Rev B 2001;63:134110.
8. Miller MK, Russell KF. J Nucl Mat 2007;371:145
9. Isobe Y, Sagisaka M, Garner FA, Fujita S, Okita T. J Nucl Mat 2009;386: 661.

10. Jiao Z, Was GS. *Acta Mater* 2011;59:1220.
11. Certain A, Voigt HJL, Allen TR, Wirth BD. *J Nucl Mat* 2013;432:281.
12. Ziegler JF, Ziegler MD, Biersak JP. *Nucl Instr Meth Phys Res B* 2010;268:1818.
13. Xu DH, Wirth BD, Li MM, Kirk MA. *Acta Mater* 2012;60:4286.
14. Xu DH, Wirth BD. *J Nucl Mat* 2010;403:184.
15. Xu DH, Hu XX, Wirth BD. *Appl Phys Lett* 2013;102:011904.
16. Monzen R, Takada K, Matsuda K. *Z Metallkd* 2003;94:1241.
17. Christien F, Barbu A. *J Nucl Mat* 2004;324:90.
18. Stoller RE et al. *Nucl Instr Meth Phys Res B* 2013;310:75.
19. Derlet PM, Nguyen-Manh D, Dudarev SL. *Phys Rev B* 2007;76:054107.
20. Soneda N, de la Rubia TD. *Phil Mag A* 1998;78:995.
21. Marian J, Wirth BD, Odette GR, Perlado JM. *Comp Mater Sci* 2004;31:347.

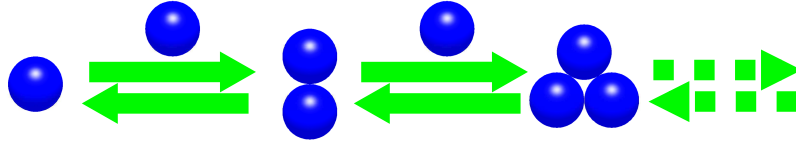


Figure 1. Illustration for Cu precipitation and re-dissolution kinetic

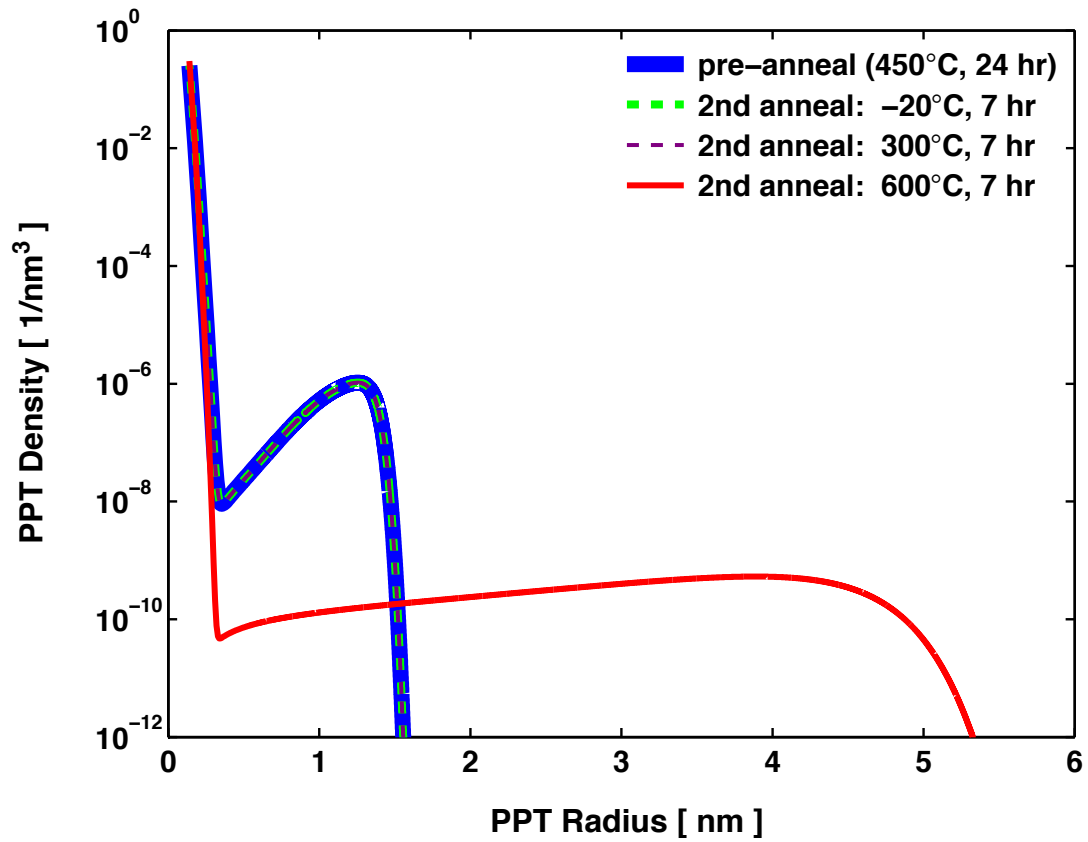


Figure 2. Number density of different sized Cu-precipitates (PPT) at the end of the pre-anneal and the three secondary anneals.

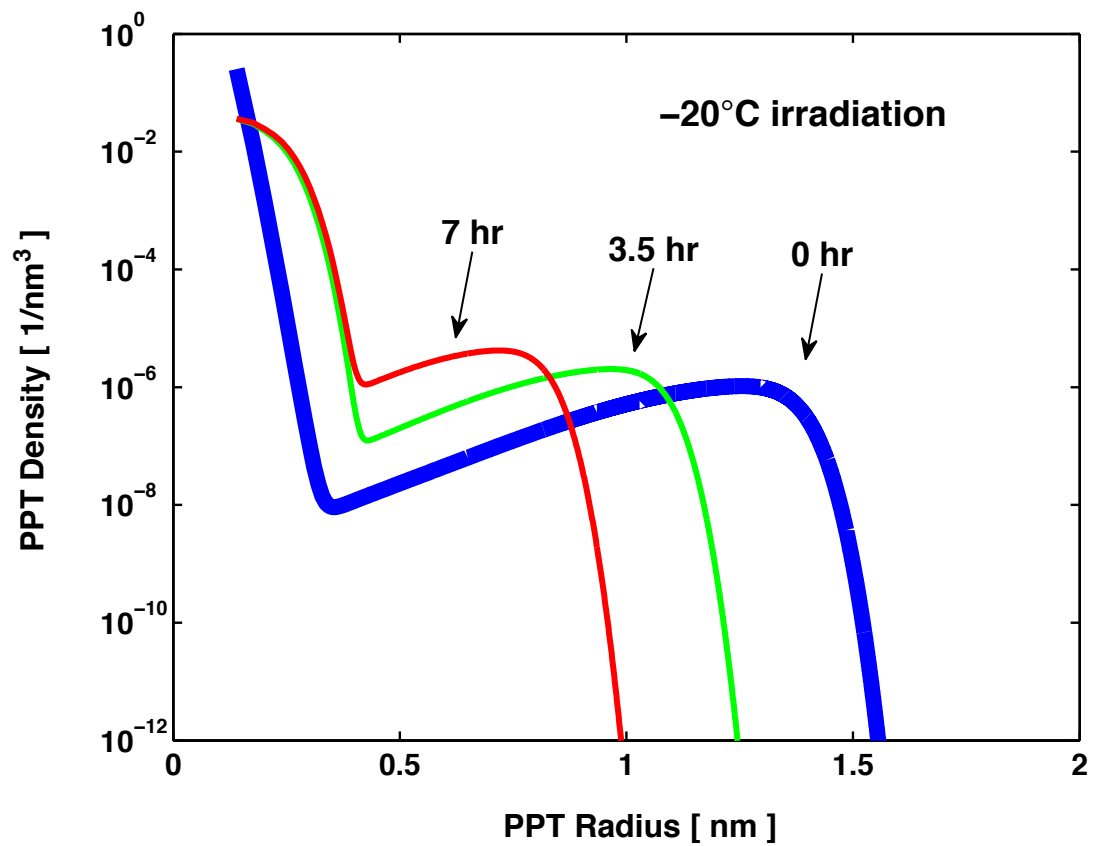


Figure 3. Model predicted evolution of precipitate number density vs. radius for the Set III specimen irradiated at -20 °C, showing re-dissolution of pre-anneal formed precipitates.

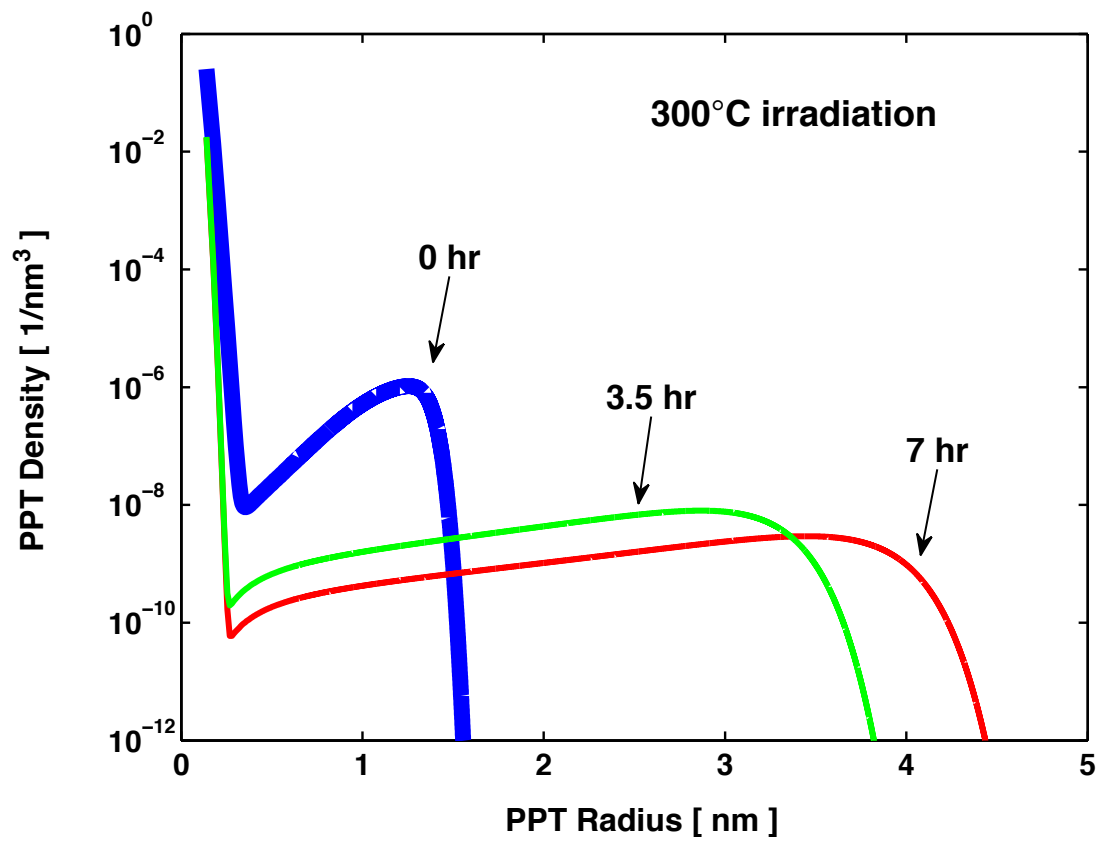


Figure 4. Model predicted evolution of precipitate number density vs. radius for the Set III specimen irradiated at 300 °C, showing coarsening of pre-anneal formed precipitates.

Table 1. Average radius and number density of Cu precipitates in different specimens, and qualitative (re-dissolved or coarsened) changes with respect to the Set I specimen, as measured by atom probe tomography. Included in the square brackets are small angle neutron scattering data also available for the Set I specimen. Temperatures in the first column are for the secondary anneals after the pre-anneal.

Specimen/history	Average radius (nm)	Number density (nm⁻³)	Change with respect to Set I
Set I	1.3 [0.9]	5.1×10^{-4} [9×10^{-4}]	NA
Set II, -20 °C	1.3	5.1×10^{-4}	no change
Set II, 300 °C	1.3	5.1×10^{-4}	no change
Set II, 600 °C	none	none	(?)
Set III, -20 °C	0.6	3.8×10^{-4}	re-dissolved
Set III, 300 °C	2.5	3.5×10^{-5}	coarsened
Set III, 600 °C	none	none	(?)

(Set I: pre-anneal only; Set II: pre-anneal plus secondary anneal; Set III: pre-anneal, secondary anneal, plus irradiation)

Table 2. Model predicted average radius and number density of Cu precipitates at the end of the pre-anneal of the Set I specimen and the secondary anneals of the Set II specimens, and qualitative (re-dissolved or coarsened) changes with respect to the Set I specimen. Temperatures in the first column are for the secondary anneals.

Specimen/history	Average radius (nm)	Number density (nm⁻³)	Change with respect to Set I
Set I	1.2	6×10^{-4}	NA
Set II, -20 °C	1.2	6×10^{-4}	no change
Set II, 300 °C	1.2	6×10^{-4}	no change
Set II, 600 °C	3.7	1.6×10^{-5}	coarsened

Table 3. Key material and irradiation related quantities used in the calculation of the irradiation vacancy concentration with a separate defect cluster dynamics model as detailed in [13] (V: vacancy; I: interstitial)

Formation energy (eV)	V ₁ : 1.7; I ₁ : 4.07				
Defect monomer-to-dimer binding energy (eV)	V ₂ : 0.3; I ₂ : 0.8				
Migration energy (eV)	V ₁	I ₁ -I ₁₀		I ₁₁ -I ₂₀	
	0.8	0.1		0.1-1.1, linear ramp	
Generation rates of interstitial clusters I ₁ -I ₂₀ (1 nm ⁻³ s ⁻¹)	I ₁	I ₂	I ₃	I ₄	I ₅
	5.69×10 ⁻²	5.03×10 ⁻³	2.16×10 ⁻³	1.42×10 ⁻³	9.90×10 ⁻⁴
	I ₆	I ₇	I ₈	I ₉	I ₁₀
	6.30×10 ⁻⁴	4.05×10 ⁻⁴	1.55×10 ⁻⁴	1.26×10 ⁻⁴	0
	I ₁₁	I ₁₂	I ₁₃	I ₁₄	I ₁₅
	0	5.52×10 ⁻⁵	0	0	0
	I ₁₆	I ₁₇	I ₁₈	I ₁₉	I ₂₀
	4.09×10 ⁻⁵	0	0	0	2.06×10 ⁻⁵
Generation rates of vacancy clusters V ₁ -V ₉ (1 nm ⁻³ s ⁻¹)	V ₁	V ₂	V ₃	V ₄	V ₅
	6.93×10 ⁻²	6.10×10 ⁻³	1.55×10 ⁻³	9.36×10 ⁻⁴	5.09×10 ⁻⁴
	V ₆	V ₇	V ₈	V ₉	
	0	0	0	2.56×10 ⁻⁴	

Table 4. Model predicted average radius and number density of Cu precipitates at the end of the pre-anneal of the Set I specimen and the irradiation of the Set III specimens, and qualitative (re-dissolved or coarsened) changes with respect to the Set I specimen. Temperatures in the first column are for the irradiation.

Specimen/history	Average radius (nm)	Number density (nm⁻³)	Change with respect to Set I
Set I	1.2	6×10^{-4}	NA
Set III, -20 °C	0.7	5.6×10^{-4}	re-dissolved
Set III, 300 °C	3.2	4.9×10^{-5}	coarsened
Set III, 600 °C	13.6	3.6×10^{-7}	coarsened